Global Radiative Convective Equilibrium with a Slab Ocean: SST Contrast, Sensitivity and Circulation

Dennis L. Hartmann[1], **Brittany D. Dygert**[1]

[1]Department of Atmospheric Sciences, University of Washington, Seattle, Washington 98195

Key Points:

- The sensitivity of global climate is reduced when the SST contrast increases with global mean temperature.
- The reduction in sensitivity is related to weakening of the greenhouse effect by increasing SST contrast.
- The large-scale circulation consists of shallow and deep cells that both strengthen as the climate warms and the SST contrast increases.

Corresponding author: Dennis L. Hartmann, dhartm@uw.edu

Abstract

Warming experiments with a uniformly insolated, non-rotating climate model with a slab ocean are conducted by increasing the solar irradiance. As the global mean surface temperature warms from the current global mean surface temperature of 289K, the surface temperature contrast between the warm-rising and cool-subsiding regions decreases to a small value at around 298K, then increases with further warming. The growing surface temperature contrast is associated with reduced climate sensitivity, mostly due to reduced strength of the greenhouse effect in the subsiding region. The clouds in the convective region are always more reflective than those in the subsiding region and this difference increases as the climate warms, acting to reduce the surface temperature contrast. At lower temperatures between 289K and 298K the shortwave suppression of SST contrast increases faster than the longwave enhancement of SST contrast. At warmer temperatures between 298K and 309K the longwave enhancement of SST contrast with warming is stronger than the shortwave suppression of SST contrast, so that the SST contrast increases. Above 309K the greenhouse effect in the subsiding region begins to grow, the SST contrast declines and the climate sensitivity increases. The transitions at 298K and 309K can be related to the increasing vapor pressure path with warming. The mass circulation rate between warm and cool regions consists of shallow and deep cells. Both cells increase in strength with SST contrast. The lower cell remains connected to the surface, while the upper cell rises to maintain a roughly constant temperature.

Plain Language Summary

A global model of a non-rotating Earth with an ocean that stores heat but does not transport it is run to energy balance with different values of globally uniform solar heating. Despite the global uniformity of the system, it develops regions of warm sea surface temperature where rain and rising motion occur, and cooler regions with downward, subsiding air motion where rainfall does not occur. These contrasts between rainy and dry regions look very similar to what is observed in the present-day tropics. As the climate is changed from current tropical temperatures toward warmer temperatures, the warm regions warm faster, mostly because the rising regions contain more water vapor. In this range of global temperatures the climate of this simple model is much less sensitive to increased solar heating than outside this range. These changes in climate sensitivity are shown to arise from well-understood physical processes that are expected to operate in nature.

1 Introduction

Sea surface temperature (SST) contrast within the tropics has received increasing interest because of its apparent role in the pattern effect on climate sensitivity (Zhou et al., 2016; Andrews et al., 2018) and because the maximum tropical SST plays such an important role in setting the state of the tropical atmosphere, which has near global effects (Dong et al., 2019). The interaction of the atmosphere with the tropical ocean currents can have a large impact on the SST structure within the tropics. Climate models suggest that weakening of the strength of tropical overturning with warming can project strongly onto the east-west Walker Circulation in the tropical Pacific ocean, leading to variations in the strength of upwelling in the equatorial Pacific (Knutson & Manabe, 1995; Vecchi & Soden, 2007). A weakening of the Walker Circulation with warming might lead to a reduction in the SST contrast, but other arguments suggest that SST contrast associated with tropical upwelling should increase in a warming Earth (Clement et al., 1996; Kohyama et al., 2017; Seager et al., 2019).

In this study we use a slab ocean model and thus dispense with effects related to ocean heat transports to focus on basic thermodynamic mechanisms for controlling tropical SST contrast. These mechanisms include the differential greenhouse effect between

warm/moist and cool/dry regions, the cloud feedbacks in the rising and subsiding regions, and the movement of energy between the warm and cool regions by atmospheric transport. These mechanisms have been studied individually previously, but a global climate model allows the interactions among them to be studied. The enhanced greenhouse effect in moist regions of the tropics was studied in observations and radiative transfer modeling by Inamdar & Ramanathan (1994). Pierrehumbert (1995) used a two-box modeling framework to show the importance of dry regions of the tropics for stabilizing the greenhouse effect feedback within the tropics. Ramanathan & Collins (1991) used observations to show that tropical ice clouds associated with convection shade the warm regions of the tropics and proposed that this would provide an upper limit on tropical SST. Increasing high cloud albedo over warm water in a warming climate would act to suppress warm SST values. Miller (1997) used a box model to investigate how increased lower tropospheric stability in a warmed tropics could increase low clouds and thereby reduce the sensitivity of climate. Enhanced low cloud in the subsiding region acting on its own would increase the SST contrast. Bony et al. (2016) argue that deep convective cloud fraction declines with SST due to increasing stability with decreasing pressure at cloud top, while Held & Soden (2006) argue that basic thermodynamic constraints require the convective mass flux to decline in a warming climate. The average cloud top temperature in the convective region is predicted to remain roughly constant during climate change (Hartmann & Larson, 2002). Becker & Wing (2020) have compared the implied climate sensitivities of a number of global climate models and cloud-resolving models in radiative-convective equilibrium (RCE) with fixed and uniform SST. They find a wide range of climate feedback parameters resulting mostly from differences in low cloud feedbacks and the development of dry, subsiding regions that change the longwave feedback.

Studying the interactions among the thermodynamic mechanisms described above requires a model that can produce a state-of-the-art simulation of the interaction between large-scale circulation and the radiative processes associated with low boundary layer clouds in the subsiding region and deep convective clouds in the region of rising motion. Convection-permitting models with horizontal resolution of the order of 1 km can operate without the use of a convection parameterization, but this resolution may not be sufficient to simulate the eddies that are critical for boundary layer clouds or anvil ice clouds. These models are generally not tuned to current observations, as global climate models are, and they are not converged, in the sense that different models produce a range of behaviors on key metrics that are as wide as those of of global climate models (Wing et al., 2020). Finally, to simulate the interaction of convection with large-scale circulation in a convection-permitting model requires a substantial investment in computational resources. For these reasons we believe it is useful to investigate these interactions with a global climate model with horizontal resolution of the order of 100km, since these models have been validated against observations and are much more computationally efficient, even though some of the critical physical processes are represented with imperfect parameterizations. To focus more specifically on the processes operating within the tropics, we make the insolation uniform and set the rotation to zero. The simulations are thus a radiative convective equilibrium (RCE) calculation in a model in which SST can respond at large scale.

The tropical atmosphere exhibits regions of consistently active deep convection, where the SST is generally higher and the free troposphere is more humid, and regions where deep convection is rare, the air is dry, and the SST is slightly lower. The tropical ocean has large regions where the SST is high and relatively uniform, especially in the western Pacific and Indian Ocean regions. Much of the deep tropical convection occurs in this 'warm pool' region. The horizontal energy exchanges between the warm pool and other regions of the tropics are generally small ($\sim$ 35 Wm^{-2}) compared to the vertical exchanges of energy between the surface, the atmosphere and space ($\sim$ 300 Wm^{-2}), so

radiative-convective equilibrium (RCE) is a useful approximate model of the tropical and even the global climate (Manabe & Wetherald, 1967).

RCE has been studied with one-dimensional models, with limited-domain cloud-resolving models and with global general circulation models (GCM). High-resolution models in a limited domain can be a means of studying the detailed physics of tropical convection and have revealed the tendency of convection to aggregate within a portion of a sufficiently large model domain (Bretherton et al., 2005; Cronin & Wing, 2017; Held et al., 1993; Tompkins, 2001a). RCE simulations have also been done with models in which the convection is parameterized (Held et al., 2007; Larson & Hartmann, 2003b,a; Arnold & Putman, 2018). Investigating RCE in climate models with parameterized convection is done with several goals in mind (e.g. Wing et al. (2018)). One goal is to better understand how the parameterizations within the models perform in such simulations (Reed et al., 2021). In addition, more fundamental understanding of how the climate system works might be gained if it can be shown that the behaviors of interest result from fundamental physical constraints that are not too dependent on the details of the parameterizations used in the models. It is this second goal that we pursue in this study.

Simulations of RCE with global climate models (GCM) can be performed with fixed sea surface temperatures (SST) (Coppin & Bony, 2015; Held et al., 2007; Retsch et al., 2019) or with a slab ocean, for which the SST interacts with atmospheric processes (Popke et al., 2013; Reed et al., 2015). In these simulations the convection aggregates in a portion of the model domain in a fashion similar to cloud-resolving models. The self-aggregation process seems to be associated with a preference for convection to be located in regions that have already been moistened by convection, where radiative and microphysical interactions will favor further convection (Bretherton et al., 2005; Tompkins, 2001b; Wing & Emanuel, 2014).

The radiative effect of water vapor and cloud variations can lead spontaneously to organized regions of upward and downward motion connected by a large-scale circulation (Nilsson & Emanuel, 1999; Raymond, 2000; Coppin & Bony, 2015; Arnold & Putman, 2018). In the absence of rotation, gravity waves can quickly spread the effect of convective heating over a large area to make stability differences between convective and non-convective regions small (Bretherton & Smolarkiewicz, 1989), but the relative size of the moist upward and dry downward regions in equilibrium depends on energetic constraints (Held & Soden, 2006). Emanuel et al. (2014) developed a theory of an instability that causes a region of uniform SST to separate into subsiding dry regions and rising regions with moist convection. The primary mechanism of this instability is the radiative effect of the contrast between moist boundary layer and dry upper tropospheric air.

When an SST gradient is imposed, a large-scale circulation flows from warm to cold regions (Raymond, 1994). The circulation that develops is strongly influenced by radiative interations (Grabowski et al., 2000) and may include multiple cells (Yano, Grabowski, & Moncrieff, 2002; Yano, Moncrieff, & Grabowski, 2002). Convective self aggregation can cause the scale and shape of the organized circulations to differ from that of the underlying SST (Müller & Hohenegger, 2020).

In a model with an interactive slab ocean, the ocean tends to be warm under the enhanced water vapor and cool elsewhere. This convection-SST interaction results in the organization becoming stronger and taking larger spatial and temporal scales. One particular case of interest is a "Tropical-World" (TW) simulation in which the planet does not rotate and the insolation is globally uniform. When done with a slab ocean model, these simulations typically develop large-scale persistent regions where SST is high and convection is common, and regions where SST is lower and convection is unlikely, much like the observed tropics (Popke et al., 2013; Reed et al., 2015). These simulations typically also have a limit cycle in which the SST contrast and the degree of aggregation

oscillate at periods that depend on the mean SST and the depth of the mixed layer (Coppin & Bony, 2017). Coppin & Bony (2018) studied the interaction between SST gradients and convective aggregation in the LMDZ5A GCM in TW configuration. Their work emphasizes the role of aggregation and SST contrast in cooling the climate. They find that aggregation cools the climate compared to a non-aggregated state, but that once aggregated, interactions between the SST gradients and clouds increase the sensitivity of the climate to CO_2 increases. They attribute this to enhanced positive low cloud feedbacks.

In this study we will consider TW simulations with the GFDL AM2.1 model with a slab ocean. We will focus primarily on the processes that determine the SST contrast in the equilibrated climate of the model, and the effect of SST contrast on climate sensitivity. In particular, we wish to better understand the mechanisms whereby the SST, atmospheric circulation, evaporation and clouds interactively self-regulate. We will argue that these mechanisms are relevant to the observed tropical climate. The advantage of using a global slab ocean model for these simulations is that the SST, clouds and large-scale circulation can fully interact, albeit without the effects of ocean currents and land-sea contrasts.

We find that SST contrast affects equilibrium climate sensitivity primarily through the greenhouse effect. In contrast to the results of Coppin & Bony (2018), low clouds play a more passive role in the determination of global sensitivity for the GCM we use here when global mean SST is similar to the current tropics. SST contrast grows in the range of SST from 298K to 309K and this results in a reduction of climate sensitivity in this range, which is mostly related to the effect of SST contrast on the globally-integrated greenhouse effect feedback. The transition to lower sensitivity above 298K is related to the growing strength of the greenhouse effect, which grows at different rates in the warm and cold regions, especially for warmer climates. For mean SST values between 298K and 309K the global mean SST is about 25 percent as sensitive to insolation changes as it is for colder or warmer mean SSTs. This decreased sensitivity arises because the mean temperature of the atmosphere increases faster than the mean temperature of the surface in this range of temperatures, and most of Earth's emission arises from the atmosphere.

The transition to higher sensitivity above 309K is related to the increasing strength of the greenhouse effect in the cool region as the integrated water vapor pressure becomes high and the efficiency of the cold region 'radiator fin' declines. The transition to higher climate model sensitivities above about 310K has been noted by previous authors (Meraner et al., 2013; Russell et al., 2013), but the transition to lower sensitivity around 298K has not been previously described. Below 298K the greenhouse effect contrast between regions of upward and downward motion is not strong enough to overcome the higher cloud albedo in the region of upward motion so that the SST contrast declines with increasing temperature. Above 298K the greenhouse effect contrast grows faster than the albedo contrast so that the SST contrast increases with warming. When the SST exceeds 309K the climate becomes more sensitive because the greenhouse effect feedback in the subsiding region becomes more strongly positive and the SST contrast declines. The shortwave cloud effect feedback acts to reduce the SST contrast at all SSTs tested, and cloud albedo contrast continues to strengthen above 310K and helps to reduce the SST contrast at the warmest temperatures.

Another feature of the simulations is the mass circulation that connects the warm and cold SST regions. At cold temperatures a single cell exists, but at higher temperatures it separates into deep and shallow circulations. The shallow circulation is associated with radiative cooling in the lower troposphere of the subsiding region, and the upper cell is associated with radiative cooling in the upper troposphere. The mass circulation in both these cells increases with global mean SST up to about 309K, beyond which they decline with the decreasing SST contrast. The mass circulations increase with

global mean SST despite the increasing dry static stability with warming. This is because the cooling rates in the downward region increase and the fraction of the domain that is occupied by subsidence increases with warming. SST gradients, static stability and diabatic heating thus interact in determining the strength and structure of these circulations.

The model and experiments are described in Section 2. The model climate is compared to observations of Earth's tropics in Section 3. Section 4 shows how the mean properties of the climate vary with global mean SST and diagnoses how SST contrasts are maintained and how this relates to the model's climate sensitivity. Section 6 uses the cooling-to-space approximation to provide an explanation for the transitions between low and high climate sensitivity at particular global mean SST values. Section 7 introduces SST-area coordinate representations of the spatial structure of large-scale circulation, relative humidity and clouds, and the diabatic processes that drive the circulation. A brief discussion of the low cloud response to warming is given in Section 8, and conclusions are summarized in section 9.

2 Model and Experimental Description

The model used is GFDL's CM2.1 Global Coupled Climate Model with a slab ocean model (Anderson et al., 2004; Delworth et al., 2006). The rotation rate is set to zero and the insolation is globally uniform. CO_2 is set to 324 ppm and CH_4 to 1650 ppb. Ozone is fixed to the observed tropical mean profile as a function of pressure. A horizontal spatial resolution of 2°latitude by 2.5°longitude, 32 vertical levels, and a time step of 900 seconds were used for the control experiments. The vertical spacing is less than 25hPa in the boundary layer, and is nearly identical to the 24-level CM2.1 vertical resolution used for CMIP5. An additional 8 levels have been added in the upper troposphere and stratosphere to better represent the extreme warming simulations included here. Experiments were also conducted with 64 vertical levels, and with 24 vertical levels and increased horizontal resolution. While increased resolution changes the mean SST, the basic conclusions about the responses to warming we reach here are not affected. The 64-level simulations produce the same dependence of mass circulation on mean SST as the 32-level simulations, and a similar transition to higher sensitivity and lower SST contrast around 310K, for example. It is very likely that some model behavior is sensitive to the details of the cloud and convection parameterizations, so our conclusions should be tested with other climate models and cloud-resolving models, but that is beyond the scope of the present work.

A set of eleven basic experiments were completed using a 50-meter slab ocean depth and incoming solar irradiance corresponding to the annual and diurnal averages at latitudes of 26°, 28°, 30°, 33°, 36°, 38°, 40°, 42°, 43°, 44°and 45°: giving four hot climates, three with SST similar to the current Tropics and four cooler climates culminating in one with a surface temperature similar to current global average of 289K (Table 1). Each experiment was run long enough to produce 40 years of stable climate for analysis after an initial spin up period that depends on the mixed-layer depth and starting climate. These experiments are denoted by their approximate global mean SST. For example, the control experiment with an insolation of 342 Wm^2 and SST of 302.1K is called "C302". If the slab ocean is reduced to 12-meter depth the model has more high frequency variability, but the basic features emphasized here are present. We have also done some experiments to test how the model behavior is different if it is forced with CO_2 increases rather than insolation increases. Some modest differences appear, but the equilibrated climates discussed here are mostly controlled by hydrologic feedbacks that depend more on the mean temperature change than on the means by which that temperature change is forced (see Supplementary Material).

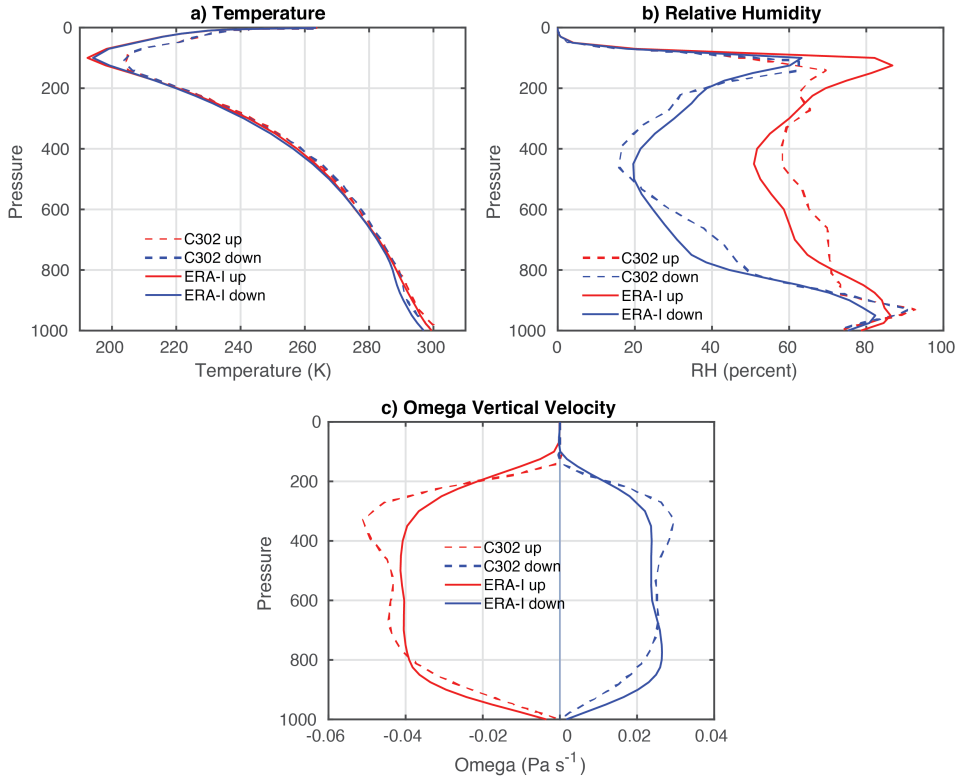

Figure 1. Comparison of a) Temperature, b) Relative humidity and c) vertical motion profiles versus pressure (hPa) in regions of upward and downward motion for the average of monthly mean fields from ERA-Interim Reanalysis in the region within 22.5S to 22.5N and 90E to 270E, and the global average of monthly means for the C302 experiment, which has a global mean SST closest to the observed tropics.

3 Comparison to Observed Tropics

In this section we explore how accurately TW emulates the observed Tropics for cases with similar SST to the current tropics, *e.g.* C302. Despite their simplifications, TW simulations have some basic characteristics in common with the observed tropics, so that, apart from the effect of ocean currents, we can argue they are a plausible analog to the observed tropics for our purposes. In particular, the vertical structure of temperature, relative humidity and mean vertical motion are important for what we want to investigate, and those very closely resemble the observed tropics.

To compare the model output to observations we use monthly SST data from NOAA OI interpolated data (Reynolds et al., 2007), radiation budget observations from CERES EBAF version 4 (Loeb et al., 2018). Atmospheric data and surface turbulent fluxes are from the ERA-Interim product (Dee et al., 2011). The period of overlap used is from March 2000 until October of 2018. Figure 1a shows that the temperature profile in the TW simulation is similar to that in the real tropics. The inversion in the subsiding region is stronger and closer to the surface in the model compared to observations, but the air temperature contrast in the boundary layer is smaller. The tropopause is warmer in the model, probably because the model does not have a Brewer-Dobson circulation in the stratosphere (Birner, 2010). The relative humidity in both the model and the observations is determined by transitioning linearly from relative humidity above water to relative humidity above ice in the temperature range from 0 to -20°C. The relative humidity dis-

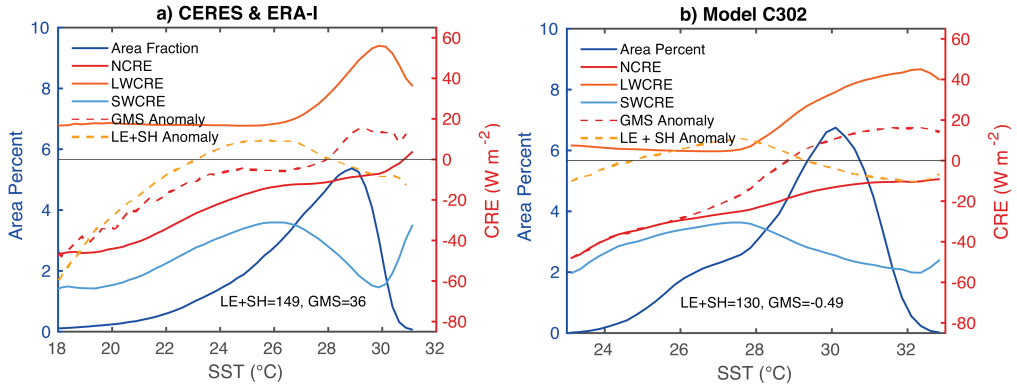

Figure 2. Area fraction occupied by SST values, Cloud Radiative Effects (CRE), heating of the atmosphere by turbulent fluxes of latent and sensible heat at the surface (LE+SH), and vertically integrated export of energy by atmospheric motions (GMS). Turbulent fluxes and atmospheric export are plotted as anomalies from the area average over all SST values. a) CRE from CERES and energy fluxes ERA-Interim reanalysis for the region from the ocean regions between 22S-22N, b) the same quantities from the model run C302, which has a mean SST close to the observed Tropics of Earth.

tribution is similar to observations in the upward and downward regions to within 10%. The lower humidity at the tropopause in the upward region may again have to do with the absence of a Brewer-Dobson Circulation.

The vertical velocity structures in the upward and downward regions also agree with observations. The vertical velocity increases rapidly away from the surface, stays relatively constant and then decreases rapidly above 300hPa. Later we will show that this structure is associated with a two-cell structure of the mass circulation. The shallow cell is associated with the lower boundary and the deeper cell is associated with the radiative cooling of the upper troposphere. Vertical motion is similar to observations in the upward and downward regions, indicating that the fraction of area that is subdsiding is also similar to the observed tropics.

Figure 2 shows that the model has a similar negatively-skewed SST distribution as the real tropics, although the negative tail is not as long, likely because of upwelling regions within the tropical oceans. The longwave and shortwave cloud radiative effects (LWCRE and SWCRE) increase toward the warmest SST, but their sum, the net cloud radiative effect (NCRE) is much weaker and does not vary much within the warm pool. Over the warmest water the net cloud radiative effect is small, negative and almost independent of SST, although more negative than in the observations. The cloud radiative effects do not become smaller at the highest SST values as in the observations. This is likely because in observations the highest SST regions tend to occur where cloud and precipitation are consistently suppressed by large-scale circulations associated with fixed geographical features such as land and sea distributions (Waliser & Graham, 1993). Those fixed constraints do not exist in TW, where high SST regions quickly attract convection and clouds, which cool the surface and suppress the positive tail of the SST distribution.

Also shown on Figure 2 are the cooling of the surface by turbulent fluxes of latent (LE) and sensible (SH) heat and the net export of energy in the atmosphere (GMS). The turbulent cooling of the surface declines toward the maximum SST values, while the atmospheric energy export peaks at the warmest temperatures. The observed tropical atmosphere exports about 35 Wm^{-2} to the extratropics but the net atmospheric export

of energy in TW is zero. The mean export of energy (GMS) from the regions of upward motion in TW is about 20 Wm^{-2} and declines for the warmest climates (Table 1).

Case	SST	Insol	T_{dif}	Pcp	SF	RH	OLR	Alb	RHR	GMS	T_{up}-T_{dn}
C289	288.7	307.2	6.1	2.8	0.58	48.9	234.7	0.24	-0.76	18.4	1.5
C295	294.8	315.2	3.3	3.1	0.61	50.3	244.2	0.22	-0.79	25.2	0.3
C297	297.3	319.1	2.4	3.3	0.60	50.2	250.0	0.22	-0.82	21.8	0.1
C298	298.0	322.9	3.0	3.4	0.61	47.1	252.8	0.22	-0.85	22.9	0.2
C300	299.7	332.8	5.0	3.7	0.61	47.3	258.4	0.22	-0.92	23.2	0.9
C302	302.1	342.4	7.0	4.2	0.63	46.9	267.0	0.22	-1.03	24.2	1.8
C304	303.6	349.3	8.0	4.5	0.65	45.9	271.5	0.22	-1.10	22.3	2.5
C307	306.8	364.4	9.8	5.1	0.67	44.6	284.7	0.22	-1.28	14.0	3.7
C309	309.2	376.3	11.2	5.6	0.67	43.6	295.1	0.22	-1.42	11.2	4.6
C313	313.2	383.6	8.8	6.1	0.68	43.0	306.7	0.21	-1.56	8.9	3.1
C319	319.0	390.5	6.4	6.4	0.75	43.0	317.8	0.19	-1.71	-1.2	1.6

Table 1. Temperatures are in Kelvin, insolation is in Wm^{-2}, precipitation (Pcp) is in mm day^{-1}, SF is subsiding fraction, RH is relative humidity in percent averaged over mass, RHR is radiative heating rate in $Kday^{-1}$, averaged over mass, GMS is the atmospheric transport from the region of upward motion in Wm^{-2}.

4 Mean Properties versus SST

In this section we describe the response of various global mean properties to global mean SST. Table 1 shows some climatological mean values for the eleven cases. The global albedo remains constant at about 22% for global mean SST between 295K and 309K, then declines for warmer SST values. Relative humidity declines slowly with warming, while subsiding fraction increases. Subsiding fraction is determined from the monthly- and mass-averaged pressure velocity.

Figure 3a shows insolation as a function of SST. From this we can infer that the climate of TW is less sensitive by a factor of 4 between surface temperatures of 298K and 309K than it is for temperatures outside this range. These changes in sensitivity are related to changes in Tdif, the SST difference of the top 20% by area of SST values from the bottom 20% of SST values, as well as the difference between the SST in regions where the mass-averaged velocity is upward and downward (Figure 3b). The decreased sensitivity aligns with increases in Tdif with mean SST.

The model sensitivity can be calculated from the values in Table 1 by taking the ratio of the mean SST change to the forcing for the C309 and C302 cases. Since the albedo remains constant at 22%, we can compute the forcing as the change in insolation multiplied by 0.78, the fraction of that change in insolation that is absorbed, giving a forcing of 26.45Wm^{-2}. The global mean SST change is 7.1K, so that the sensitivity parameter is 7.1K/(26.45Wm^{-2}) = 0.27 K/(Wm^{-2}), which means it takes almost 4Wm^{-2} of forcing to warm the SST by 1K in the range where SST contrast is increasing. The sensitivity estimated from the difference between C295 and C298 is 1 K/(Wm^{-2}), about a factor of 4 larger. Since the albedo is relatively constant in this range, it cannot be shortwave cloud feedbacks or their response to SST contrast that explain the changed sensitivity. We next explore what processes explain the increase in SST contrast and how this is related the reduced climate sensitivity.

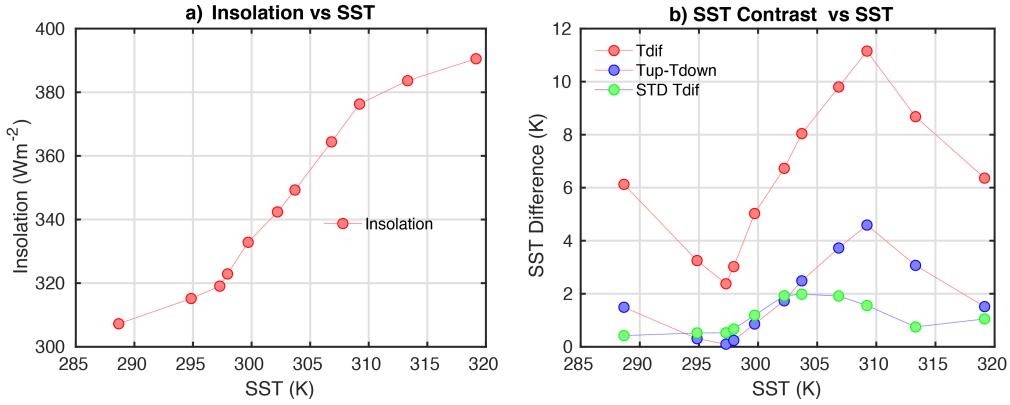

Figure 3. a) Insolation as a function of SST, b) SST contrast as a function of mean SST, Tdif is the difference between the warmest and coldest 20% of SST values, Tup-Tdown is the SST difference between regions of upward and downward motion. The standard deviation with time of the monthly mean Tdif is also shown.

4.1 Diagnosis of SST contrast changes

To explore SST contrast we need first to consider the basic budgets of the top-of-atmosphere (TOA), atmosphere (ATM) and surface (SFC). The relevant balance for the TOA is,

$$\dot{E}_{TOA} = R_{TOA} - GMS \tag{1}$$

where $\dot{E}_{TOA}$ represents the storage of energy, $R_{TOA} = R_{net}$ is the net radiation input at TOA and GMS is the 'Gross Moist Stability', the total export of energy from a column by atmospheric motions, all in units of Wm^{-2}. For the atmosphere, the balance is,

$$\dot{E}_{ATM} = R_{ATM} - GMS + (LE + SH) \approx 0 \tag{2}$$

where LE+SH is the sum of the upward turbulent fluxes of latent and sensible energy at the surface, and R_{ATM} is the mass-integrated radiative heating of the atmosphere, which is always negative. At the surface the balance is,

$$\dot{E}_{SFC} = R_{SFC} - (LE + SH) \tag{3}$$

An important constraint on the system is that $\dot{E}_{TOA} \approx \dot{E}_{SFC}$.

4.2 Energetics of SST Contrast

The contrasts in the terms in the energy balance between regions of upward and downward motion are an indicator of the factors determining the SST contrast. As a measure how the differences in SST between the upward and downward regions are maintained we consider the differences in the TOA and SFC balances between the upward and downward regions, which are shown in Figure 4. The net balance at TOA is $TOA.Bal = \dot{E}_{TOA}$, indicated by the black stars in Figure 4. The radiation term is divided into solar and terrestrial components. It is reasonable to expect the cloud albedo in regions of upward motion to be larger than the cloud albedo in downward regions. For this reason solar radiation always acts to decrease the SST contrast, and this influence increases with SST. At temperatures below 298K this shortwave influence dominates and the SST contrast declines as the difference in net radiation declines until the SST contrast between regions of upward and downward motion is near zero. We see in Figure 4a that the TOA net radiation contrast grows with increasing SST between 298K and 309K because the OLR contrast effect on SST difference becomes more positive faster than the

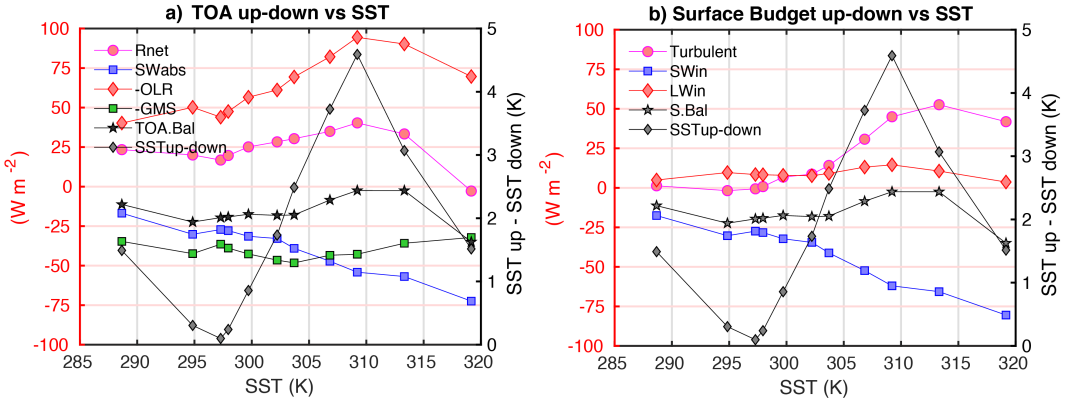

Figure 4. Difference in energy balance components between the upward and downward regions for a) TOA and b) SFC (left axis). Right axis shows the SST difference of upward minus downward regions.

absorbed shortwave contrast effect becomes more negative. This confirms that it is the greater increase of the greenhouse effect over the warm pool that causes the SST difference to increase in this range. Beyond 309K the OLR contrast declines while the shortwave contrast acts more strongly to decrease the SST contrast.

At the surface (Figure 4b) the increase of SST contrast between 298K and 309K is marked by an increase in the contrast of the turbulent fluxes, which are dominated by the latent cooling of the surface, which increases more over the subsiding region with warming than over the rising region. Weaker evaporation over the warm regions is a feature of the observed tropics that is reproduced by the model (Figure 2). Because of (3) the surface turbulent fluxes are strongly constrained by the surface radiation balance, which is largely determined by the shortwave effect of clouds in the atmosphere.

Because we have sorted by the vertical velocity, the balance indicated by the stars in Figure 4 tends to be negative, always acting to decrease the SST contrast between upward and downward regions. The vertical velocity, convective clouds and net atmospheric export of energy respond to the SST contrast such that where the vertical velocity is strongly upward, the SST is being suppressed. The region of warm SST attracts convection which then acts to suppress the warmest SST.

Figure 5a shows that the net cloud radiative effect (NCRE) also exhibits distinct kinks near 298K and 309K, particularly in the subsiding region. Between 298K and 309K the NCRE becomes more negative with increasing SST, but the difference between the NCRE in the upward and downward regions changes by only about 10 Wm^{-2} in this range, much less than the change in the GHE difference and in the wrong direction to explain the growth in SST contrast, with the NCRE in the rising motion becoming more negative faster than the NCRE in the downward region as the climate warms. Beyond 309K the NCRE in the downward region becomes more positive as the low cloud fraction and associated albedo decline with warming there. We will show later that at these high temperatures the radiative cooling of the boundary layer becomes less efficient due to the increasing vapor pressure path, and radiative cooling of the lower atmosphere is a prime driver of low clouds over the ocean. Entrainment drying and other mechanisms may also suppress low clouds at high temperatures (Bretherton, 2015).

Figure 5b shows the shortwave cloud radiative effect (SWCRE) normed by the insolation, so that it represents the opposite of the albedo enhancement due to clouds. In the subsiding region the cloud reflection shows a small decrease near the point where the

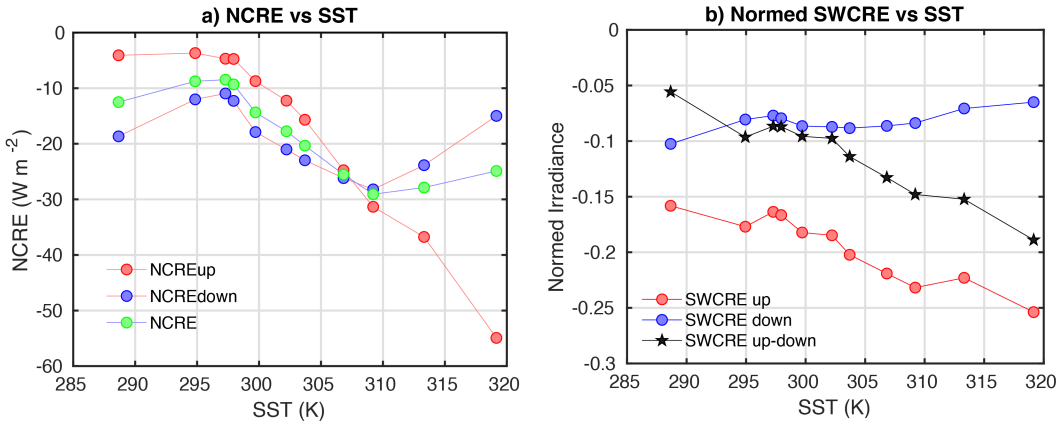

Figure 5. a) Net cloud radiative effect (NCRE) for upward, downward and global regions and b) shortwave cloud radiative effect (SWCRE) normalized by insolation and functions of SST. Black stars indicate the difference between upward and downward regions.

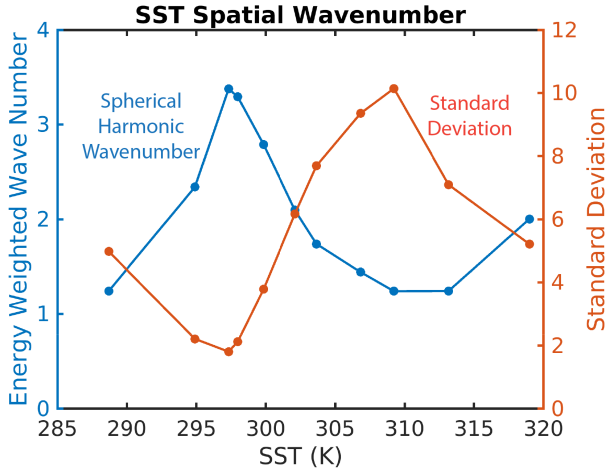

Figure 6. Variance-weighted spherical wavenumber (left scale) and globally averaged local standard deviation of SST (right scale).

SST contrast is minimum, and another decrease at temperatures above 309K. Between 300K and 309K the cloud abedo enhancement in the subsiding region remains fairly constant. The cloud albedo enhancement is stronger in the rising region and increases fairly steadily with increasing SST, apart from some slight albedo reductions near 298K and 309K. The black stars in Figure 5b show that the cloud albedo is always larger in the region of rising motion, and this difference generally increases with temperature. The cloud albedo contrast thus always acts to decrease the SST contrast, and more strongly with increasing SST between 298K and 309K where the SST contrast is increasing with SST.

4.3 Spatial Scale of SST Variations

The spatial scale of the SST patterns is near global. Figure 6 shows the variance-weighted spherical harmonic wavenumber and globally-averaged local standard deviation of monthly SST as functions of SST for the eleven cases. The global mean is first removed from each month before the spatial variance is computed. A spherical harmonic

expansion is performed of each month's global SST pattern. The squared real amplitude of each spherical harmonic amplitude is then multiplied by the spherical harmonic wavenumber, integrated over all spherical harmonics and divided by the total variance to form a variance weighted characteristic wavenumber averaged over the final 480 months of integration. When the SST contrast is large the average spherical harmonic wavenumber is close to 1 meaning that the dominant structure of the SST distribution is nearly as large as it can be, with a positive anomaly in one hemisphere and a negative anomaly in the other. When the SST contrast goes through a minimum around 298K the spherical harmonic wavenumber becomes larger, indicating smaller scales accompany the lower variance.

4.4 Summary of SST Contrast Maintenance

To summarize this section, we note that the cloud albedo contrast between upward and downward regions acts to reduce the SST contrast and this effect increases in magnitude with increasing mean SST. The decrease in SST contrast between 289K and 298K occurs because the negative cloud albedo effect on SST contrast increases faster with SST than the OLR contrast. In this low-temperature regime the effect of moisture contrast on OLR contrast is relatively weak. Between 298K and 309K the OLR contrast between the warm-upward and cool-downward regions grows faster than the albedo contrast with increasing SST and the SST contrast increases. Within this regime, the 'radiator fin' mechanism of Pierrehumbert (1995) is more important for global sensitivity than the cloud albedo mechanisms of Miller (1997) for low clouds and Ramanathan & Collins (1991) for high clouds. At temperatures warmer than 309 K the OLR contrast weakens and with it the SST contrast, since the cloud albedo effect in decreasing SST contrast continues to increase with global warming. When the SST contrast is large, its spatial scale is global, most often with just one cold and one warm center.

In the next section we will elaborate further on how the suppression of the greenhouse effect in the subsiding region contributes to both the increase in SST contrast and the stabilization of the climate in the range between 298K and 309K. Beyond 309K the greenhouse effect in the subsiding region begins to strengthen because of the increasing infrared opacity of even the dry subsiding region, and this both makes the SST difference decline and the climate sensitivity increase.

5 Greenhouse Effect and SST Contrast

The primary reason for the low sensitivity of the model is the strong sensitivity of the OLR to surface temperature of about 4 $Wm^{-2}K^{-1}$ between 298K and 309K. Consistently with the more efficient atmospheric longwave cooling, the hydrological sensitivity of $4\%K^{-1}$ is also large compared to typical global models (Pendergrass & Hartmann, 2014).

A key to understanding the insensitivity of the model is thus to consider the longwave greenhouse effect (GHE) changes. The GHE is defined here to be the difference between the longwave emission from the surface and the outgoing longwave radiation (OLR) (Inamdar & Ramanathan, 1994).

$$GHE = \sigma T_s^4 - OLR \tag{4}$$

Here σ is the Stefan-Boltzmann constant and T_s is the surface temperature. Figure 7a shows the GHE in the upward and downward regions for clear and average conditions. Between mean SSTs of 298K and 309K the greenhouse effect in the subsiding region remains roughly constant, meaning that the OLR increases at about the same rate as the surface emission. This is a reflection of the stabilizing effect of the dry 'radiator fins' as described by Pierrehumbert (1995), but also of the effect of SST contrast under a tropical atmosphere. The subsiding region atmospheric temperatures increase at the same

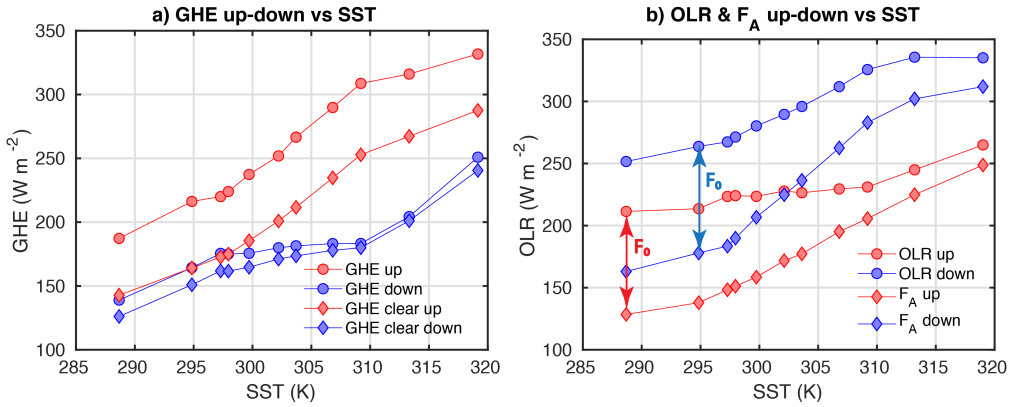

Figure 7. a) Greenhouse effect in upward and downward regions for all-sky and clear-sky conditions, b) OLR and atmospheric cooling rate contribution to OLR from F_A and F_0 in the upward and downward regions as a function of global mean SST. F_0 is the difference between OLR and F_A, as indicated by the arrows.

rate as the rising region temperatures, but the relative humidity is lower and high clouds are largely absent, so that the emission to space increases rapidly with global surface temperature. Because the surface temperature in the upward region controls the atmospheric temperature and increases faster than the mean surface temperature, the mean rate of change of OLR with mean SST is large. This mechanism works better at warm temperatures, where most of the OLR is coming from the atmosphere and not the surface, but at high temperatures it breaks down when the water vapor path in the subsiding becomes sufficiently large.

The greenhouse effect is also the primary driver of the growth in SST contrast with warming. The greenhouse effect grows by $50\mathrm{Wm}^{-2}$ in the upward region, but hardly at all in the downward region between 298K and 309K (Figure 7a). At temperatures lower than 298K the GHE increases at about the same rate in the upward and downward regions, but between 298K and 309K the GHE increases much faster in the upward region. These changes are dominated by clear-sky radiative processes. In the upward region the difference between the clear-sky and all-sky GHE is almost independent of SST. This results from the fact that the emission temperature of water vapor and the emission temperature of clouds are both nearly fixed by clear-sky radiative processes and the associated control of cloud top temperature (Hartmann & Larson, 2002; Hartmann et al., 2019). Thus cloud longwave effects do not play a definitive role in the increase in SST contrast with warming, which is mostly a clear-sky radiative effect.

To understand how the greenhouse effect changes with mean temperature, it is helpful to decompose the OLR into contributions from net surface loss and atmospheric cooling. Start with the equation for the longwave cooling rate of the atmosphere as a function of the net longwave flux in the upward direction, F, where c_p is specific heat at constant pressure, ρ_{Air} is air density and z is altitude.

$$\left.\frac{dT}{dt}\right|_{LW} = -\frac{1}{\rho_{Air}\, c_p}\frac{dF}{dz} \tag{5}$$

Integrating this equation through the mass of the atmosphere after using the hydrostatic relationship we obtain,

$$OLR = F(p_s) \; - \int_0^{p_s} c_p \left. \frac{dT}{dt} \right|_{LW} \frac{dp}{g} \tag{6}$$

$$= \quad F_0 \quad + \quad F_A \tag{7}$$

The OLR thus consists of two terms; the net longwave flux upward at the surface (F_0), plus the mass integral of the longwave radiative cooling rate (F_A). Figure 7b shows the OLR and the contribution to the OLR from the atmospheric cooling rate, F_A , for the upward and downward regions. The difference between OLR and F_A is the surface contribution F_0. In the region of rising motion, because the relative humidity is so high and clouds are present, the OLR does not increase very much in the range of temperatures between 298K and 309K. This is mostly because the net longwave loss at the surface is declining rapidly, primarily as a result of increased water vapor continuum absorption in the window region (e.g. Hartmann (2016), Fig. 10.10 and Koll & Cronin (2018)). The atmospheric cooling rate increases almost linearly with temperature across the entire range of SST values. The atmospheric temperature where emission occurs stays about the same, as it is tied closely to water vapor, but as the surface warms the emission temperature moves to a lower pressure where it can more easily be transmitted to space so that the cooling rate increases (Hartmann et al., 2021) .

Figure 7b shows that in the region of subsiding motion the cooling rate of the atmosphere, F_A, increases more rapidly than in the region of upward motion, again principally because of the relative humidity distribution, but also because the air temperature is linked very closely to that in the region of rising motion, where it approximates a moist adiabat tied to the near-surface temperature. The net surface radiation loss decreases with increasing SST, but the emission from the atmosphere increases sufficiently fast to overcome this effect so that OLR increases at the same rate as the surface emission. The insensitivity of the clear-sky greenhouse effect in the subsiding region to mean warming depends strongly on the SST contrast, since the atmospheric emission temperature in the subsiding region is tied to the warmer SST in the rising region. Motions quickly respond to redistribute mass to decrease pressure gradients. This dynamic balance may also explain why the air temperature above the boundary layer in the subsiding region is slightly warmer than the air temperature in the rising region, when the air temperature below the inversion is colder in the subsiding region (Fig. 1a). Above mean SST of 309K, the surface longwave loss, F_0, reaches a limiting value and the OLR must follow the linearly increasing F_A. This increases the local climate stability in the warm region. In the subsiding region the OLR stops increasing above 309K because the surface longwave loss declines, but also because the atmospheric cooling rate begins increasing much more slowly with increasing SST.

6 Cooling-to-Space Interpretation

In this section we use to cooling-to-space approximation to provide a physical explanation for the transitions in the behavior of the model at 298K and 309K. The cooling-to-space approximation is known to be excellent for water vapor emission in the atmosphere (Jeevanjee & Fueglistaler, 2020a). Hartmann et al. (2021) showed the cooling-to-space approximation in the following form, in which the result of Chou et al. (1993) that the mass absorption coefficient for water vapor scales approximately linearly with pressure has been used.

$$\left. \frac{dT}{dt} \right|_\lambda = -\left\{ \frac{0.622\,\pi}{c_p\, p_0\, \bar{\mu}} RH \;\; e_s(T)\, k_{\lambda 0}\, B_\lambda(T) \right\} e^{\frac{-\tau_\lambda}{\bar{\mu}}}. \tag{8}$$

Here $\bar{\mu} = 1.66^{-1}$ is the average over a hemisphere of $\mu = \cos\theta$, $k_{\lambda 0}$ is the mass absorption coefficient at the reference pressure p_0, RH represents relative humidity and $e_s(T)$

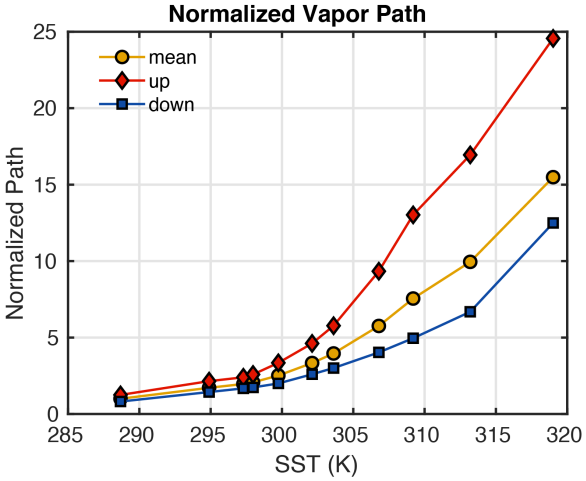

Figure 8. Vapor pressure path above 850hPa normalized by its global mean value for case C289. Values for the upward, downward and global mean values are shown.

is the saturation vapor pressure at temperature T. τ_λ is the optical depth from the given pressure to the top of the atmosphere for the wavelength λ. The part in brackets represents an emission term that depends only on temperature and relative humidity, and the exponential term represents the transmissivity of this emission to space. Using the hydrostatic equation, the optical depth can be written,

$$\tau_\lambda = \int_z^\infty k_\lambda \, \rho_{H_2O} \, dz = \frac{k_{\lambda 0} \, 0.622}{g \, p_0} \int_0^p RH \, e_s(T) \, dp. \tag{9}$$

The optical depth and the transmissivity thus depend on the mass-integrated vapor pressure, or the vapor pressure path,

$$VPP = \int_0^p RH \, e_s(T) \, dp. \tag{10}$$

The cooling rate for a particular wavelength of radiation, λ, peaks where the scaled optical depth is one $\tau_\lambda / \bar{\mu} \approx 1.0$. Using this constraint to solve for $k_{\lambda 0}$, and substituting that result into (8), we obtain,

$$\frac{dT}{dt}\Big|_\lambda \approx -\left\{ \frac{e^{-1} \, \pi \, g}{c_p} \, RH \;\; e_s(T) \;\; B_\lambda(T) \right\} VPP^{-1}. \tag{11}$$

The peak cooling rate for an emission line is thus given by a term that depends only on the temperature and relative humidity at the level of emission divided by the vapor pressure path above that level (VPP). The cooling of the atmosphere by water vapor is provided by a spectrum of emission lines that pass through optical depth one at different levels of the atmosphere (Harries, 1997; Jeevanjee & Fueglistaler, 2020b). At low pressures the cooling rate can increase because VPP becomes small (Hartmann et al., 2021), but if VPP becomes very large this can weaken the cooling rate because the emission cannot escape the atmosphere. At high temperatures, where the moist adiabatic lapse rate is small and the vapor pressure is high, the increase in VPP can suppress the radiative cooling of the lower atmosphere, leading to radiative decoupling and eventually a runaway greenhouse effect (Leconte et al., 2013).

With these ideas in mind we plot scaled VPP for the atmosphere above 850 hPa as a function of SST in Figure 8. We choose 850hPa because at this level the air temperature is very similar in the upward and downward regions, so that the emission term

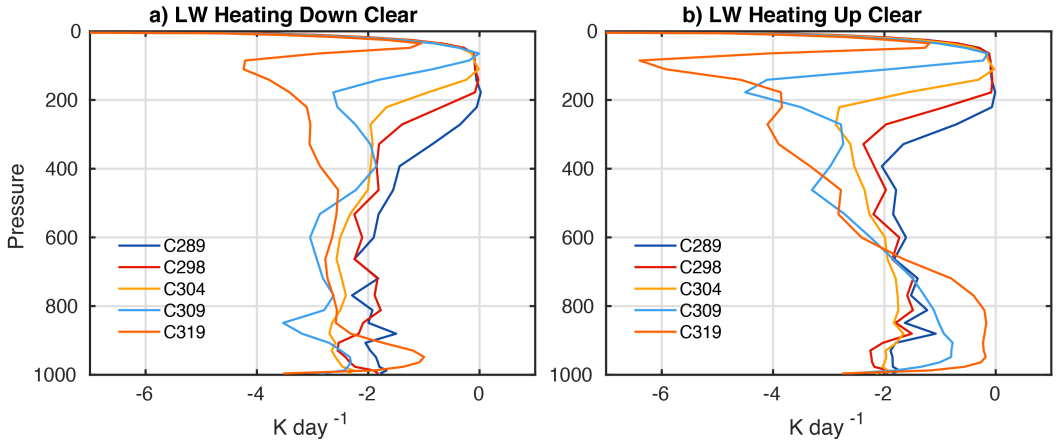

Figure 9. Clear-sky longwave heating rates for a selection of cases as functions of pressure for a) downward and b) upward regions.

in (11) should be similar, apart from small difference in relative humidity at the top of the boundary layer. This implies that the cooling rate contrast would mostly be controlled by the contrast in VPP. Since the air temperature above 850 hPa is similar in the upward and downward regions, the existence of a contrast in VPP is mostly related to relative humidity. If the relative humidity contrast is fixed, the magnitude of the VPP contrast increases with temperature through the Clausius-Clapeyron dependence of saturation vapor pressure.

For SST less than 298K, VPPs in the upward and downward regions are similar, so that we expect the contrast in clear-sky cooling rate and greenhouse effect to be small. Above 298K the contrast in VPP between upward and downward regions increases. This increasing contrast of VPP between upward and downward regions increases the GHE contrast between the two regions, which drives a bigger difference in the SST between the two regions. At some point, however, the absolute value of VPP becomes large enough that cooling of the surface and lower troposphere is inhibited, which accelerates the growth in the GHE. This occurs first in the region of upward motion, where the RH and VPP are higher, but around 309K VPP in the downward region becomes large enough to inhibit cooling rates and thence the OLR. This simultaneously makes the model more sensitive and reduces the SST difference between the upward and downward regions.

To see these effects in the simulations we consider the clear-sky longwave radiative heating rates in the upward and downward regions for a selection of cases (Figure 9). These are plotted as a function of pressure so that F_A is the proportional to the area between the cooling rate line and zero. In general, the contribution of atmospheric emission to cooling (F_A) increases with warmer SST because the cooling rate increases and moves upward to encompass more atmospheric mass. At very high temperatures, however, the atmospheric cooling of the lower atmosphere decreases because the large VPP prevents the lower troposphere from cooling efficiently. This decrease in lower tropospheric cooling is most evident in the upward region (Figure 9b), but at the warmest temperatures the cooling rate in the subsiding region also declines near the surface as the SST is increased. For the warmest cases the longwave cooling rate in the lower troposphere decreases and most of the cooling comes from the upper troposphere. The atmospheric column approaches a decoupled state that would lead to a runaway greenhouse effect if the whole troposphere was as moist as the upward region (Renno, Emanuel, & Stone, 1994; Renno, Stone, & Emanuel, 1994; Leconte et al., 2013).

We thus conclude that the fundamental reason for the apparent regime changes at 298K and 309K can be understood through the dependence of the lower tropospheric cooling rate on vapor pressure path. At temperatures colder than 298K the difference in the VPP between regions of upward and downward motion is too small to produce a significant GHE contrast. Between 298K and 309K the contrast in VPP and cooling rate grows with mean SST, but beyond 309K VPP becomes large enough that the cooling in the subsiding region becomes inefficient, at which point the SST contrast declines while the sensitivity of the model climate increases.

7 Properties in SST-Area Coordinates

As suggested by Figure 2, SST is a useful coordinate to organize an analysis of these simulations. We divide the SST into 0.25K intervals and then compute the area-averaged atmospheric structure for those SST bins. Each monthly grid cell from 40 years of simulation is identified by its SST, and variables of interest such as vertical velocity, relative humidity, etc, are averaged for each SST bin, where the area of the grid cell is taken into account to produce an SST composite. Each SST bin also has a value that determines what fraction of the total area of the globe falls within the SST bin, $f_A(SST)$, which was shown in Figure 2b for case C302. The cumulative area fraction is computed by integrating this pdf of area fraction across SST.

$$F_A(SST) = \int_0^{SST} f_A(SST)\, dSST \tag{12}$$

A streamfunction can be computed by integrating the omega vertical velocity in Pa/s through area,

$$\Psi(F_A, p) = \frac{A_E}{g} \int_0^{F_A} \omega(p)\, dF'_A \tag{13}$$

Here A_E is the surface area of Earth, g is the acceleration of gravity and $\Psi(F_A, p)$ has units of kg/s. The horizontal area velocity in $m^2 s^{-1}$ flowing toward the region of warm SST is then computed from,

$$V = -g\, \frac{d\Psi}{dp} \tag{14}$$

and the pressure velocity can be obtained from

$$\omega = \frac{g}{A_E}\, \frac{d\Psi}{dF_A} \tag{15}$$

We can then plot vertical profiles of atmospheric variables in the same coordinate system of area fraction ordered by SST (Figure 10). Air temperatures are shown as anomalies from the global average at each pressure level to reveal the near constancy of air temperature above the boundary layer and the strong variations of air temperature within the boundary layer. This is because, without rotation, gravity waves quickly adjust the atmospheric temperature to be nearly equal everywhere, except over the cold region where an inversion is present and some vertical compensation by warmer air aloft is necessary to keep the surface pressure gradients small.

The relative humidity (Figure 10b), on the other hand, shows a great deal of variation across SST from less than 10% in the middle troposphere above the cooler SST to much higher values over warmer SST and near the surface and tropopause. The relative humidity is related to the vertical velocity, which is upward over the warmer SST and downward over the cooler SST (Figure 10c). Note that the strength of the mass circulation is about an order of magnitude bigger than the zonal Hadley Cell, since the Hadley

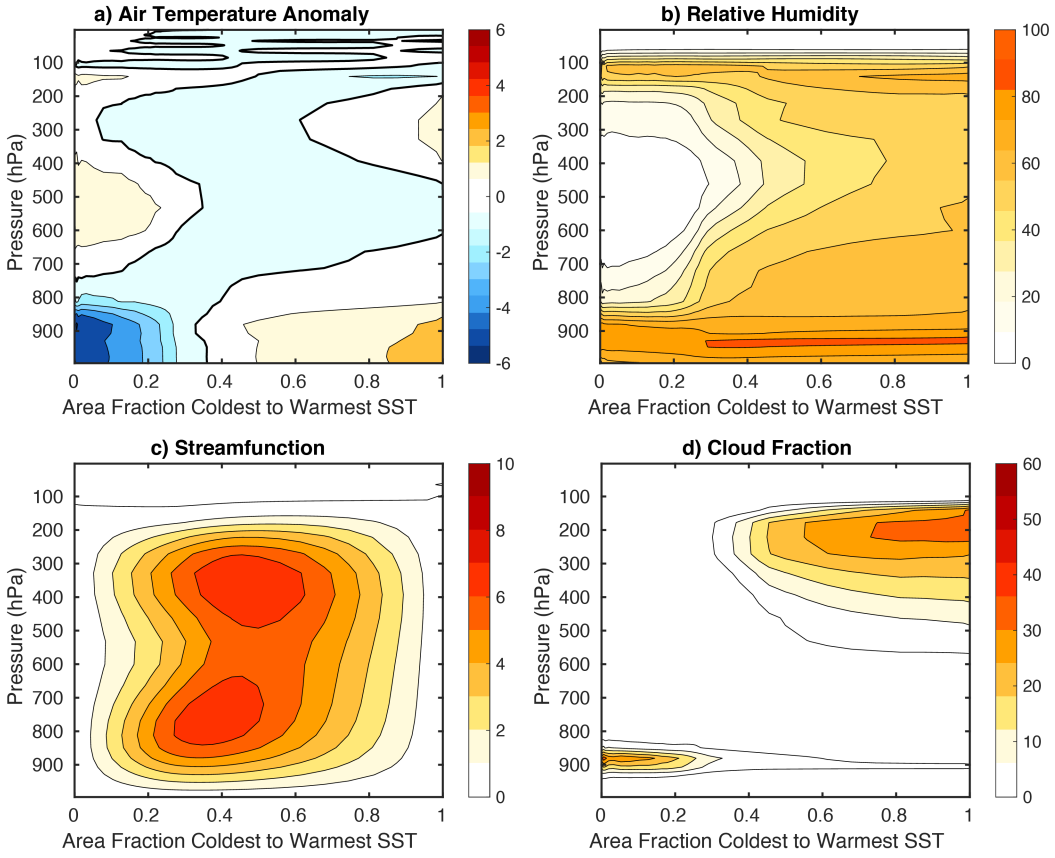

Figure 10. a) Air temperature anomaly (c.i. 1K), b) Relative humidity (c.i. 10%), c) Streamfunction (c.i. $1.0x10^{11}kgs^{-1}$) and d) Cloud Fraction (c.i. 10%) as functions of air pressure in hPa, plotted as functions of cumulative area fraction, F_A from coldest to warmest SST for case C302.

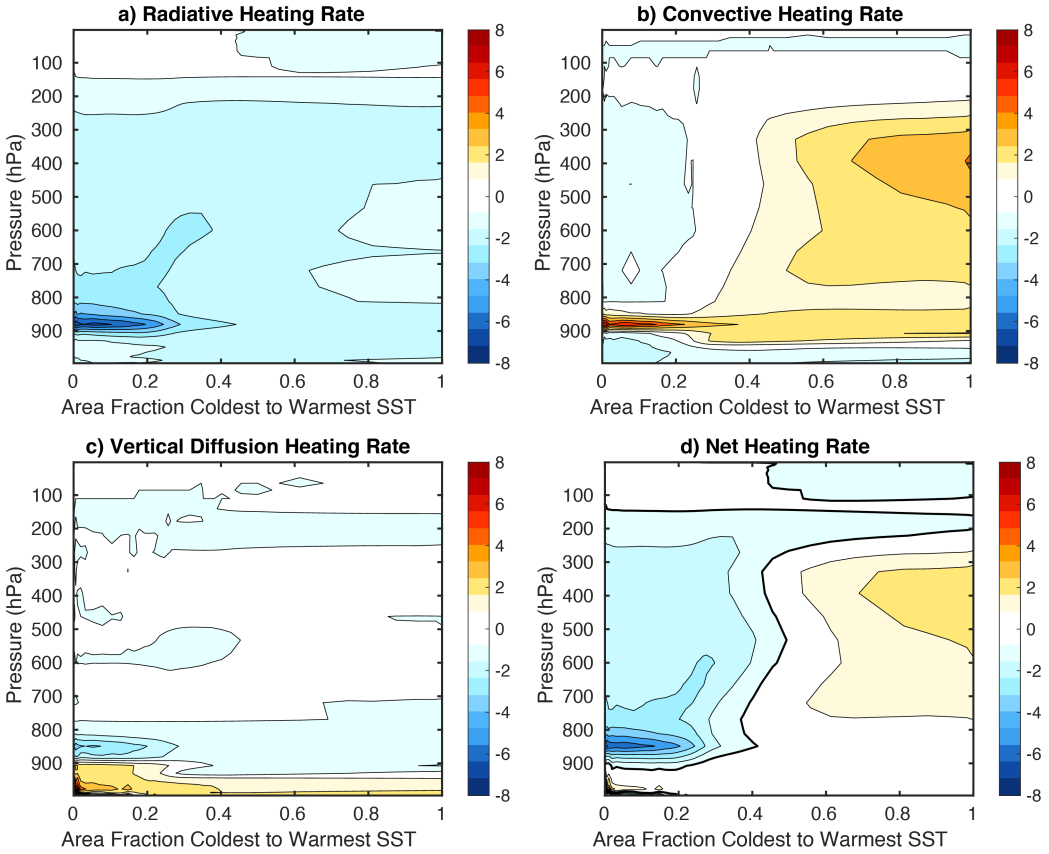

Figure 11. As in Figure 10 except a) Radiative Cooling Rate, b) Total Convective heating rate, c) Heating by Vertical Diffusion and d) Total net diabatic heating. (c.i. 1.0 $Kday^{-1}$).

Cell only incorporates the meridional mass circulation, and considerable circulation in the tropics is east-west. The circulation has two distinct maxima, one in the lower troposphere and one in the upper, with two corresponding maxima in vertical velocity over the cooler water. It is this double-cell forcing that gives the observed vertical velocity its almost square structure seen in Figure 1. Cloudiness shows large coverage by high ice clouds above the warmer SST, and boundary layer clouds in the region of coolest SST (Figure 10d).

The streamfunction can be better understood by considering the diabatic heating processes that drive it. Figure 11 shows the diabatic heating values associated with radiation, convection and vertical diffusion. The shallow circulation cell is driven by radiative cooling associated with the relative humidity gradient at and above the boundary layer top in the subsiding region, augmented by radiative cooling off the low cloud tops. The radiative cooling associated with the relative humidity gradient in the lower troposphere of the subsiding region serves to deepen the shallow circulation beyond what it would be from boundary layer processes alone. The deep circulation cell is driven by the deep radiative cooling and the compensating convective heating in the rising region.

Nigam (1997) showed that radiative cooling from stratocumulus tops could drive important shallow circulations. Zhang et al. (2004) gave evidence for the existence of such shallow circulations from reanalysis products. Nolan et al. (2007) suggested that these circulations were analogous to sea breezes driven by SST gradients. Nishant et al. (2016) used regional simulations to argue that radiative driving was a more consistent expla-

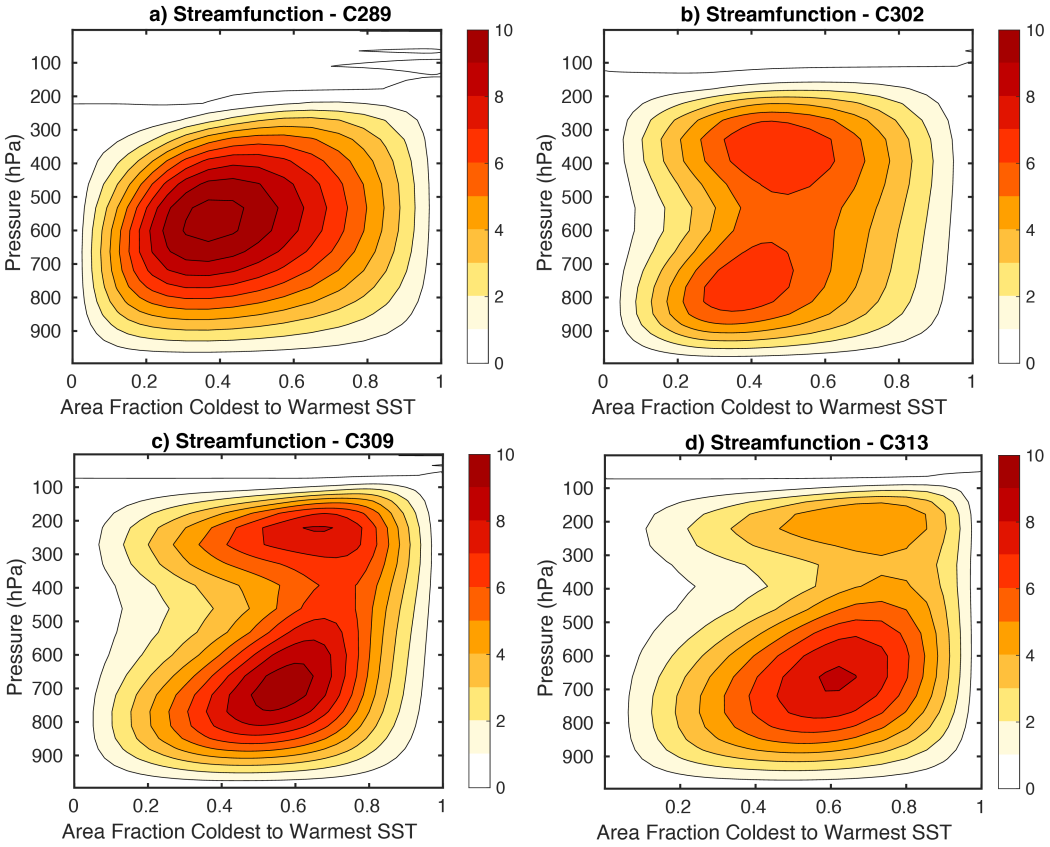

Figure 12. Streamfunction as in Figure 10 for cases a) C289, b) C302, c) C309 and d) C313. Units are kgs^{-1} and contour interval is $1x10^{11}kgs^{-1}$.

nation for the existence of these shallow circulations. Schulz & Stevens (2018) used compositing in moisture space to show that moisture gradients lead to radiative heating anomalies that drive shallow circulations. Convective heating profiles estimated from active remote sensing indicate seasons and locations where the tropical convective heating profile has two maxima in the vertical (Huaman & Takahashi, 2016; Huaman & Schumacher, 2018), as indicated for AM2.1 in Figure 11b . Our model results support the idea that radiative cooling in the subsiding region drives a shallow circulation in the tropics. In addition, we show the important role of radiative cooling from the relative humidity gradient above the boundary layer in deepening that shallow circulation, so that it is not only the moist boundary layer and the clouds within it that are important.

The change in the structure of the streamfunction with mean SST is shown in Figure 12. At relatively low temperatures such as C289 the circulation consists of a single strong overturning cell with a center in the mid-troposphere. As the SST increases, dual cells form as the boundary layer and the upper cooling cells separate (C302). This transition may be an example of the onset of instability of single cell circulations theorized by Emanuel et al. (2014). The longwave opacity of the boundary layer in the subsiding region may be below the threshold when the first internal mode circulation becomes unstable. Another possibility is that the cooling in the upper troposphere is too close to the top of the lower cell to result in two distinct circulations. C289 has a small dry and subsiding region with a strong radiative cooling rate at the top of the boundary layer near 800hPa, but the convective heating rate in the warm area peaks only slightly above that at 600hPa (not shown). With further warming the upper cell moves to lower pres-

sure, keeping the temperature of the upper cell nearly constant, while the lower cell remains attached to the surface. Both cells increase in strength as the mean SST is increased from 302K to 309K, but beyond 309K the circulations weaken, especially in the upper troposphere. The general consensus is that overturning rates should decrease in a warmed climate because the dry static stability increases, so that the radiative cooling can be balanced by a weaker subsidence rate (Knutson & Manabe, 1995; Held & Soden, 2006). In the present simulations the radiative cooling rate increases in magnitude with warming, the subsiding fraction increases slightly and the upward velocity in the region of rising motion increases, so that the mass circulation speeds up with warming, despite the fact that the mean downward vertical velocity in the subsiding region decreases a little with warming. The increasing difference of SST between the rising and subsiding region likely also contributes to the increased mass circulation. Among other effects, increased SST contrast in the tropics results in the atmosphere warming faster than the mean SST, which accelerates atmospheric radiative cooling. This enhanced cooling offsets part of the effect of increasing stability on mean subsidence rates.

8 Low Cloud Response

We next turn to the very modest changes in cloud reflectivity in the region of subsiding motion. Figure 13 shows that the cloud fraction stays about constant, and liquid water content increases only slightly in the boundary layer of the subsiding region between C302 and C309, but then declines for the warmest cases C313 and C319. The cloud fraction is approximately constant, until it decreases for SST greater than 309K. The low clouds thus thicken slightly between 302K and 309K mean SST, and this would increase the reflectivity of the low clouds. The effect of this increased cloud albedo is offset by the increased absorption of solar radiation in the atmosphere by water vapor as the SST and specific humidity increase. The insolation is also increasing, but the effect of this is minor compared to the large increases in water vapor abundance with temperature.

As the climate is warmed in these simulations, the large-scale variables that we expect to control low cloud abundance in the subsiding region also change. The lower tropospheric stability and the estimated inversion strength increase with the mean SST. The surface wind speed in the subsiding region is roughly proportional to the SST contrast, which decreases with global mean for SST values below 298K, then increases with global mean SST between 298K and 309K, and decreases again for SST greater than 309K. The wind speed at the reference level for the boundary layer averaged over the subsiding region varies by a factor of two between the minimum and maximum SST contrast from 3 ms^{-1} at minimum SST constrast to 6 ms^{-1} at maximum SST contrast. Relative humidity at the reference level increases with wind speed, which reduces the response of evaporation to wind speed.

One would expect the dynamical effect of the increased inversion strength to increase the low cloud fraction and albedo in the subsiding region (Klein & Hartmann, 1993; Wood & Bretherton, 2006; Bretherton, 2015)). As the climate warms, however, the vertical gradient of specific humidity in the lower troposphere increases very rapidly with SST. This would be expected to decrease the cloud amount through a thermodynamic mechanism discussed by Bretherton & Blossey (2014) that is related to the increased vertical gradient of moisture in warmed climates (Brient & Bony, 2013), and is believed to play an important role in explaining the wide variations in low cloud feedbacks in climate models (Sherwood et al., 2014). One would also expect increased surface wind speed to increase mixing in the boundary layer and influence low cloud coverage. Parsing the low cloud responses into contributions from inversion strength, SST and large-scale circulation and thereby explaining why the cloud albedo remains approximately constant in the subsiding region across a wide range of SST values in our simulations is beyond the scope of the present paper. Other models show a much stronger role for low cloud feedbacks in RCE simulations with slab oceans than we see in our simulations (Coppin

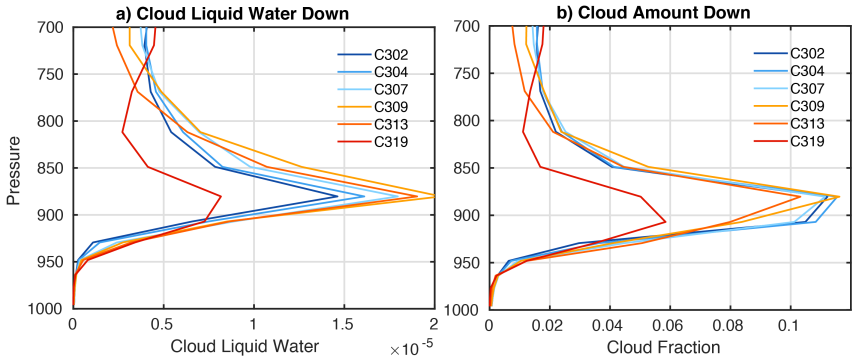

Figure 13. a) Cloud liquid water content (LWC) and b) cloud fraction below 700hPa in the region of subsiding velocity.

& Bony, 2018; Drotos et al., 2020). Simulation of low clouds remains a fundamental uncertainty in climate modeling.

9 Conclusion

We have investigated the processes that determine the mean sea surface temperature contrast in a climate model run in Tropical World mode with no rotation, uniform insolation and a slab ocean model. The mean SST difference between regions of rising and subsiding velocity at first decreases as the mean temperature increases above 289K, then increases above 298K, then decreases again for mean SST above 309K. These transitions between decreasing and increasing SST contrast are explained by the differences in the magnitude of the changes in the greenhouse effect and the shortwave cloud forcing in the upward and downward regions. Shortwave contrast increases with temperature, always acting to reduce the SST contrast, and more strongly as the climate warms. The greenhouse effect on SST contrast at first decreases more slowly, then more rapidly, then more slowly again than the shortwave cloud effect as the climate warms. These changes in the balance of feedbacks on SST contrast result in transitions in the sensivity of the climate from high to low to high as the climate warms.

The transitions in the strength of the greenhouse effect on SST contrast are explained in terms of the water vapor pressure path above the boundary layer. At low vapor pressure paths the contrast between the upward and downward regions is small so that the contrast in greenhouse effect is small. Above about 298K the contrast in vapor pressure path becomes large enough to foster a stronger greenhouse effect contrast between the upward and downward regions so that the SST contrast increases with warming. At warm enough temperatures the subsiding region achieves a stronger greenhouse effect feedback associated with a larger vapor pressure path, while the warm region begins to experience vapor pressure paths sufficient to lead to a runaway greenhouse effect. At these high temperatures the greenhouse effect contrast and SST contrast decline.

Within the SST regime where the SST contrast is increasing with global mean SST the climate is relatively insensitive, whereas outside this regime the climate is about four times more sensitive. This low sensitivity regime is associated with a very weak greenhouse effect feedback in the subsiding region. The SST in the subsiding region increases more slowly than the atmospheric temperature, and most of the OLR comes from the atmosphere at tropical temperatures, so that the OLR increases very rapidly with SST in the subsiding region.

The strength of the mass overturning circulation between the warm and the cold SST regions is a single cell at low temperatures (289K), but is split into a lower cell and an upper cell at warmer temperatures. The lower cell is associated with radiative cooling from the humidity decline at and above the boundary layer in the subsiding region where the mid-troposphere relative humidity is low. This cell remains at a fixed pressure as the climate warms. The upper cell is associated with radiative cooling near the top of the layer of rapid radiative cooling. It moves upward to lower pressures so as to maintain a relatively constant air temperature as the SST is warmed. The strengths of both circulation cells increase with warming up to a mean SST of 309K, despite the increasing dry static stability associated with the moist adiabatic lapse rate. This is possible because the area of subsiding motion increases and the radiative cooling rate increases as the SST is warmed.

In the particular model used here the global mean albedo does not change much across a wide range of SST. The albedo decreases slightly with mean SST in the subsiding region where low clouds are present and increases steadily in the region of upward motion and deep convection. The low-cloud albedo in the subsiding region does not change much with SST. One could speculate that this is because increased lower tropospheric stability with warming, which should increase low cloud albedo, is offset by thermodynamic processes, which provide more drying of the boundary layer by entrainment of air from above as the SST is increased. The structure and strength of the circulation also change with SST, and in particular the average surface wind speed in the subsiding region increases with the SST contrast. It is therefore challenging to separate the thermodynamic and dynamic influences on low cloud albedo in these experiments.

The basic mechanisms of increasing greenhouse effect and shortwave cloud radiative effect contrast between regions of upward and downward motion seem to be robust and intuitive. The exact balance between these two effects is likely to be sensitive to the parameterizations that determine the water content, ice content and fractional coverage of clouds. The increase in cloud ice and high cloud reflectivity in the model, although consistent with the elevated radiative cooling profile, are very sensitive to the parameterizations used to relate convective heating to net ice production. The relationship of radiative cooling rate to cloud ice amount is probably best undertaken with a model in which deep convection is explicitly resolved and coupled to realistic cloud microphysics. Attempts to do this show interesting interactions between cooling rate, pressure and lapse rate (Sokol & Hartmann, 2021).

The low clouds in the model are parameterized and low cloud response to warming is known to be a major cause of uncertainty in global warming simulations. The low clouds in our simulations respond only modestly to global warming. It is possible that in another model the low clouds could respond strongly to warming and be a more important driver of changed SST contrast. Finally, of course, rotation, realistic continental geography, and ocean heat transports would likely greatly modify the responses seen in TW simulations, and may alter the relative importance of water vapor, cloud and circulation feedbacks on climate change.

Acknowledgments

This work was supported by the National Science Foundation under Grant AGS-1549579 and AGS-2124496. Discussions with Peter Blossey and Qiang Fu were critical to the development of this paper. We are grateful to GFDL-NOAA for providing the GCM model code used here and for the data providers cited. Model data supporting the figures and associated software can be found here

http://hdl.handle.net/1773/46293

References

Anderson, J. L., Balaji, V., Broccoli, A. J., Cooke, W. F., Delworth, T. L., Dixon, K. W., ... Dev, G. G. A. M. (2004). The new gfdl global atmosphere and land model am2-lm2: Evaluation with prescribed sst simulations. *J. Climate*, *17*(24), 4641-4673.

Andrews, T., Gregory, J. M., Paynter, D., Silvers, L. G., Zhou, C., Mauritsen, T., ... Titchner, H. (2018). Accounting for changing temperature patterns increases historical estimates of climate sensitivity. *Geophys. Res. Lett.*, *45*(16), 8490-8499. doi: 10.1029/2018gl078887

Arnold, N. P., & Putman, W. M. (2018). Nonrotating convective self-aggregation in a limited area agcm. *J. Adv. Model. Earth Sys.*, *10*(4), 1029-1046. doi: 10.1002/2017ms001218

Becker, T., & Wing, A. A. (2020). Understanding the extreme spread in climate sensitivity within the radiative-convective equilibrium model intercomparison project. *J. Adv. Model. Earth Sys.*, *12*(10). doi: https://doi.org/10.1029/2020MS002165

Birner, T. (2010). Residual circulation and tropopause structure. *Journal of the Atmospheric Sciences*, *67*(8), 2582-2600. doi: 10.1175/2010jas3287.1

Bony, S., Stevens, B., Coppin, D., Becker, T., Reed, K., Voigt, A., & Medeiros, B. (2016). Thermodynamic control of anvil-cloud amount. *Proc. Nat. Acad. Sci. U. S. A.*, *113*(32), 8927-8932. doi: doi:10.1073/pnas.1601472113

Bretherton, C. S. (2015). Insights into low-latitude cloud feedbacks from high-resolution models. *Phil. Trans. Roy. Soc. A*, *373*(2054). doi: 10.1098/rsta.2014.0415

Bretherton, C. S., & Blossey, P. N. (2014). Low cloud reduction in a greenhouse-warmed climate: Results from lagrangian les of a subtropical marine cloudiness transition. *J. Adv. Model. Earth Sys.*, *6*(1), 91-114. doi: 10.1002/2013ms000250

Bretherton, C. S., Blossey, P. N., & Khairoutdinov, M. (2005). An energy-balance analysis of deep convective self-aggregation above uniform sst. *J. Atmos. Sci.*, *62*(12), 4273-4292.

Bretherton, C. S., & Smolarkiewicz, P. K. (1989). Gravity waves, compensating subsidence and detrainment around cumulus clouds. *J. Atmos. Sci.*, *46*(6), 740-59.

Brient, F., & Bony, S. (2013). Interpretation of the positive low-cloud feedback predicted by a climate model under global warming. *Climate Dynamics*, *40*(9-10), 2415-2431. doi: 10.1007/s00382-011-1279-7

Chou, M. D., Ridgway, W. L., & Yan, M. M. H. (1993). One-parameter scaling and exponential-sum fitting for water vapor and CO_2 infrared transmission functions. *J. Atmos. Sci.*, *50*(14), 2294-2303.

Clement, A. C., Seager, R., Cane, M. A., & Zebiak, S. E. (1996). An ocean dynamical thermostat. *J. Climate*, *9*(9), 2190-2196.

Coppin, D., & Bony, S. (2015). Physical mechanisms controlling the initiation of convective self-aggregation in a general circulation model. *J. Adv. Model. Earth Sys.*, *7*(4), 2060-2078. doi: 10.1002/2015ms000571

Coppin, D., & Bony, S. (2017). Internal variability in a coupled general circulation model in radiative-convective equilibrium. *Geophys. Res. Lett.*, *44*(10), 5142-5149. doi: 10.1002/2017gl073658

Coppin, D., & Bony, S. (2018). On the Interplay Between Convective Aggregation, Surface Temperature Gradients, and Climate Sensitivity. *J. Adv. Model. Earth Sys.*, *10*(12), 3123–3138. doi: 10.1029/2018MS001406

Cronin, T. W., & Wing, A. A. (2017). Clouds, circulation, and climate sensitivity in a radiative-convective equilibrium channel model. *J. Adv. Model. Earth Sys.*, *9*(8), 2883-2905. doi: 10.1002/2017ms001111

Dee, D. P., Uppala, S. M., Simmons, A. J., Berrisford, P., Poli, P., Kobayashi, S., ... Vitart, F. (2011). The era-interim reanalysis: configuration and performance of

the data assimilation system. *Quart. J. Royal Met. Soc.*, *137*(656), 553-597. doi: 10.1002/qj.828

Delworth, T. L., Broccoli, A. J., Rosati, A., Stouffer, R. J., Balaji, V., Beesley, J. A., ... Zhang, R. (2006). Gfdl's cm2 global coupled climate models. part i: Formulation and simulation characteristics. *J. Climate*, *19*(5), 643-674. doi: 10.1175/jcli3629.1

Dong, Y., Proistosescu, C., Armour, K. C., & Battisti, D. S. (2019, June). Attributing Historical and Future Evolution of Radiative Feedbacks to Regional Warming Patterns using a Green's Function Approach: The Preeminence of the Western Pacific. *J. Climate*, *32*(17), 5471–5491. doi: 10.1175/JCLI-D-18-0843.1

Drotos, G., Becker, T., Mauritsen, T., & Stevens, B. (2020). Global variability in radiative-convective equilibrium with a slab ocean under a wide range of co2 concentrations. *Tellus A*, *72*(1), 1-19. doi: 10.1080/16000870.2019.1699387

Emanuel, K., Wing, A. A., & Vincent, E. M. (2014). Radiative-convective instability [Journal Article]. *J. Adv. Mod. Earth Sys.*, *6*(1), 75-90. doi: 10.1002/2013ms000270

Grabowski, W. W., Yano, J. I., & Moncrieff, M. W. (2000). Cloud resolving modeling of tropical circulations driven by large-scale sst gradients. *J. Atmos. Sci.*, *57*(13), 2022-2039. doi: 10.1175/1520-0469(2000)057⟨2022:Crmotc⟩2.0.Co;2

Harries, J. E. (1997). Atmospheric radiation and atmospheric humidity. *Quart. J. Royal Meteorol. Soc.*, *123*(544), 2173-86.

Hartmann, D. L. (2016). *Global physical climatology* (2nd ed.). Elsevier.

Hartmann, D. L., Blossey, P., & Dygert, B. (2019). Convection and climate: What have we learned from simple models and simplified settings? *Curr. Clim. Change Rep.*, *5*(3), 196-206. doi: 10.1007/s40641-019-00136-9

Hartmann, D. L., Dygert, B. D., Blossey, P. N., Fu, Q., & Sokol, A. B. (2021). The vertical profile of radiative cooling in radiative-convective equilibrium: Moist adiabat versus entrainment-modified plume model. *J. Climate*, submitted.

Hartmann, D. L., & Larson, K. (2002). An important constraint on tropical cloud-climate feedback. *Geophys. Res Lett.*, *29*(20), 1951-1954. doi: doi:10.1029/2002GL015835

Held, I. M., Hemler, R. S., & Ramaswamy, V. (1993). Radiative-convective equilibrium with explicit two-dimensional moist convection. *J. Atmos. Sci.*, *50*(23), 3909-3927.

Held, I. M., & Soden, B. J. (2006). Robust responses of the hydrological cycle to global warming. *J. Climate*, *19*(21), 5686-5699.

Held, I. M., Zhao, M., & Wyman, B. (2007). Dynamic radiative-convective equilibria using gcm column physics. *J. Atmos. Sci.*, *64*(1), 228-238.

Huaman, L., & Schumacher, C. (2018). Assessing the vertical latent heating structure of the east pacific itcz using the cloudsat cpr and trmm pr. *J. Climate*, *31*(7), 2563-2577. doi: 10.1175/jcli-d-17-0590.1

Huaman, L., & Takahashi, K. (2016). The vertical structure of the eastern pacific itczs and associated circulation using the trmm precipitation radar and in situ data. *Geophys. Res. Lett.*, *43*(15), 8230-8239. doi: 10.1002/2016gl068835

Inamdar, A. K., & Ramanathan, V. (1994). Physics of greenhouse effect and convection in warm oceans. *J. Climate*, *7*(5), 715-31.

Jeevanjee, N., & Fueglistaler, S. (2020a). On the cooling-to-space approximation. *J. Atmos. Sci.*, *77*(2), 465-478. doi: 10.1175/jas-d-18-0352.1

Jeevanjee, N., & Fueglistaler, S. (2020b). Simple spectral models for atmospheric radiative cooling. *J. Atmos. Sci.*, *77*(2), 479-497. doi: 10.1175/jas-d-18-0347.1

Klein, S., & Hartmann, D. (1993). The seasonal cycle of low stratiform clouds. *J. Climate*, *6*(8), 1587-1606.

Knutson, T. R., & Manabe, S. (1995). Time-mean response over the tropical pacific to increased co2 in a coupled ocean-atmosphere model. *J. Climate*, *8*(9),

2181-2199.

Kohyama, T., Hartmann, D. L., & Battisti, D. S. (2017). La nina-like mean-state response to global warming and potential oceanic roles. *J. Climate*, *30*(11), 4207-4225. doi: 10.1175/jcli-d-16-0441.1

Koll, D. D. B., & Cronin, T. W. (2018). Earth's outgoing longwave radiation linear due to H2O greenhouse effect. *Proc. Nat. Acad. Sci. U. S. A.*, *115*(41), 10293-10298. doi: 10.1073/pnas.1809868115

Larson, K., & Hartmann, D. L. (2003a). Interactions among cloud, water vapor, radiation, and large-scale circulation in the tropical climate. part ii: Sensitivity to spatial gradients of sea surface temperature. *J. Climate*, *16*(10), 1441-1455.

Larson, K., & Hartmann, D. L. (2003b). Interactions among cloud, water vapor, radiation, and large-scale circulation in the tropical climate. part i: Sensitivity to uniform sea surface temperature changes. *J. Climate*, *16*(10), 1425-1440.

Leconte, J., Forget, F., Charnay, B., Wordsworth, R., & Pottier, A. (2013). Increased insolation threshold for runaway greenhouse processes on earth-like planets. *Nature*, *504*(7479), 268-271. doi: 10.1038/nature12827

Loeb, N., Doelling, D. R., Wang, H., Su, W., Nguyen, C., Corbett, J., ... Kato, S. (2018). Clouds and the earth's radiant energy system (CERES) energy balanced and filled (EBAF) top-of-atmosphere (TOA) edition-4.0 data product. *J. Climate*, *31*(15 January 2018), 895-918. doi: doi.org/10.1175/JCLI-D-17-0208.1

Manabe, S., & Wetherald, R. (1967). Thermal equilibrium of the atmosphere with a given distribution of relative humidity. *J. Atmos. Sci.*, *24*, 241-259.

Meraner, K., Mauritsen, T., & Voigt, A. (2013). Robust increase in equilibrium climate sensitivity under global warming [Journal Article]. *Geophys. Res. Lett.*, *40*(22), 5944-5948. doi: 10.1002/2013gl058118

Miller, R. (1997). Tropical thermostats and low cloud cover. *J. Climate*, *10*(3), 409-440.

Müller, S. K., & Hohenegger, C. (2020). Self-aggregation of convection in spatially varying sea surface temperatures. *J. Adv. Model. Earth Sys.*, *12*(1), e2019MS001698. doi: https://doi.org/10.1029/2019MS001698

Nigam, S. (1997). The annual warm to cold phase transition in the eastern equatorial pacific: diagnosis of the role of stratus cloud-top cooling. *J. Climate*, *10*(10), 2447-67.

Nilsson, J., & Emanuel, K. A. (1999). Equilibrium atmospheres of a two-column radiative-convective model. *Q. J. Roy. Meteor. Soc.*, *125*(558), 2239-2264.

Nishant, N., Sherwood, S. C., & Geoffroy, O. (2016). Radiative driving of shallow return flows from the itcz. *J. Adv. Model. Earth Sys.*, *8*(2), 831-842. doi: 10.1002/2015ms000606

Nolan, D. S., Zhang, C., & Chen, S. H. (2007). Dynamics of the shallow meridional circulation around intertropical convergence zones. *J. Atmos. Sci.*, *64*(7), 2262-2285. doi: 10.1175/jas3964.1

Pendergrass, A. G., & Hartmann, D. L. (2014). The atmospheric energy constraint on global-mean precipitation change. *J. Climate*, *27*(2), 757-768. doi: 10.1175/jcli-d-13-00163.1

Pierrehumbert, R. (1995). Thermostats, radiator fins and the local runaway greenhouse. *J. Atmos. Sci.*, *52*, 1784-1806.

Popke, D., Stevens, B., & Voigt, A. (2013). Climate and climate change in a radiative-convective equilibrium version of echam6. *J. Adv. Model. Earth Sys.*, *5*(1), 1-14. doi: 10.1029/2012ms000191

Ramanathan, V., & Collins, W. (1991). Thermodynamic regulation of ocean warming by cirrus clouds deduced from observations of the 1987 el nino. *Nature*, *351*(6321), 27-32.

Raymond, D. J. (1994). Convective processes and tropical atmospheric circulations. *Q. J. Roy. Meteorol. Soc.*, *120*(520), 1431-1455. doi: 10.1002/qj.49712052002

Raymond, D. J. (2000). The hadley circulation as a radiative-convective instability. *J. Atmos. Sci.*, *57*(9), 1286-1297. doi: 10.1175/1520-0469(2000)057⟨1286:Thcaar⟩2.0.Co;2

Reed, K. A., Medeiros, B., Bacmeister, J. T., & Lauritzen, P. H. (2015). Global radiative-convective equilibrium in the community atmosphere model, version 5. *J. Atmos. Sci.*, *72*(5), 2183-2197. doi: 10.1175/jas-d-14-0268.1

Reed, K. A., Silvers, L. G., Wing, A. A., Hu, I.-K., & Medeiros, B. (2021). Using radiative convective equilibrium to explore clouds and climate in the community atmosphere model [Journal Article]. *J. Adv. Model. Earth Sys.*, *13*(12), e2021MS002539. doi: https://doi.org/10.1029/2021MS002539

Renno, N. O., Emanuel, K. A., & Stone, P. H. (1994). Radiative-convective model with an explicit hydrologic cycle. 1. formulation and sensitivity to model parameters. *J. Geophys. Res.*, *99*(D7), 14429-41.

Renno, N. O., Stone, P. H., & Emanuel, K. A. (1994). Radiative-convective model with an explicit hydrologic cycle. 2. sensitivity to large changes in solar forcing. *J. Geophys. Res.*, *99*(D8), 17001-20.

Retsch, M. H., Mauritsen, T., & Hohenegger, C. (2019). Climate change feedbacks in aquaplanet experiments with explicit and parametrized convection for horizontal resolutions of 2,525 up to 5 km. *J. Adv. Mod. Earth Sys.*, *11*(7), 2070-2088. doi: 10.1029/2019ms001677

Reynolds, R. W., Smith, T. M., Liu, C., Chelton, D. B., Casey, K. S., & Schlax, M. G. (2007). Daily high-resolution-blended analyses for sea surface temperature. *J. Climate*, *20*(22), 5473-5496. doi: 10.1175/2007jcli1824.1

Russell, G. L., Lacis, A. A., Rind, D. H., Colose, C., & Opstbaum, R. F. (2013). Fast atmosphere-ocean model runs with large changes in co2 [Journal Article]. *Geophys. Res. Lett.*, *40*(21), 5787-5792. doi: 10.1002/2013gl056755

Schulz, H., & Stevens, B. (2018). Observing the tropical atmosphere in moisture space. *J. Atmos. Sci.*, *75*(10), 3313-3330. doi: 10.1175/jas-d-17-0375.1

Seager, R., Cane, M., Henderson, N., Lee, D. E., Abernathey, R., & Zhang, H. H. (2019). Strengthening tropical pacific zonal sea surface temperature gradient consistent with rising greenhouse gases. *Nature Climate Change*, *9*(7), 517-+. doi: 10.1038/s41558-019-0505-x

Sherwood, S. C., Bony, S., & Dufresne, J. L. (2014). Spread in model climate sensitivity traced to atmospheric convective mixing. *Nature*, *505*(7481), 37-+. doi: 10.1038/nature12829

Sokol, A. B., & Hartmann, D. L. (2021). Radiative cooling, latent heating and cloud ice in the tropical upper troposphere [Journal Article]. *J. Climate*. doi: https://doi.org/10.1175/JCLI-D-21-0444.1

Tompkins, A. M. (2001a). On the relationship between tropical convection and sea surface temperature. *J. Climate*, *14*(5), 633-637. doi: 10.1175/1520-0442(2001)014⟨0633:otrbtc⟩2.0.co;2

Tompkins, A. M. (2001b). Organization of tropical convection in low vertical wind shears: The role of water vapor. *J Atmos. Sci.*, *58*(6), 529-545. doi: 10.1175/1520-0469(2001)058⟨0529:ootcil⟩2.0.co;2

Vecchi, G. A., & Soden, B. J. (2007). Global warming and the weakening of the tropical circulation. *J. Climate*, *20*(17), 4316-4340. doi: 10.1175/jcli4258.1

Waliser, D., & Graham, N. (1993). Convective cloud systems and warm-pool sea surface temperatures: coupled interactions and self-regulation. *J. Geophys. Res. Atmos.*, *98*(D7), 12881-93.

Wing, A. A., & Emanuel, K. A. (2014). Physical mechanisms controlling self-aggregation of convection in idealized numerical modeling simulations. *J. Adv. Model. Earth Sys.*, *6*(1), 59-74. doi: 10.1002/2013ms000269

Wing, A. A., Reed, K. A., Satoh, M., Stevens, B., Bony, S., & Ohno, T. (2018). Radiative-convective equilibrium model intercomparison project. *Geosci. Model*

Dev., *11*(2), 793-813. doi: 10.5194/gmd-11-793-2018

Wing, A. A., Stauffer, C., Becker, T., Reed, K., Ahn, M., Arnold, N., ... al., e. (2020). Clouds and convective self-aggregation in a multi-model ensemble of radiative-convective equilibrium simulations. *J. Adv. Mod. Earth Sys.*. doi: https://doi.org/10.1029/2020MS002138

Wood, R., & Bretherton, C. S. (2006). On the relationship between stratiform low cloud cover and lower-tropospheric stability. *J. Climate*, *19*(24), 6425-6432.

Yano, J. I., Grabowski, W. W., & Moncrieff, M. W. (2002). Mean-state convective circulations over large-scale tropical sst gradients. *J. Atmos. Sci.*, *59*(9), 1578-1592. doi: 10.1175/1520-0469(2002)059⟨1578:Msccol⟩2.0.Co;2

Yano, J. I., Moncrieff, M. W., & Grabowski, W. W. (2002). Walker-type mean circulations and convectively coupled tropical waves as an interacting system. *J. Atmos. Sci.*, *59*(9), 1566-1577. doi: 10.1175/1520-0469(2002)059⟨1566:Wtmcac⟩2.0.Co;2

Zhang, C. D., McGauley, M., & Bond, N. A. (2004). Shallow meridional circulation in the tropical eastern pacific. *J. Climate*, *17*(1), 133-139.

Zhou, C., Zelinka, M. D., & Klein, S. A. (2016). Impact of decadal cloud variations on the earth's energy budget. *Nature Geoscience*, *9*(12), 871-+. doi: 10.1038/ngeo2828